

Supporting Information for  
**Mapping crustal shear wave velocity structure and radial  
anisotropy beneath West Antarctica using seismic ambient  
noise**

J. P. O'Donnell<sup>1</sup>, A. M. Brisbourne<sup>2</sup>, G. W. Stuart<sup>1</sup>, C. K. Dunham<sup>1</sup>,  
Y. Yang<sup>3</sup>, G. A. Nield<sup>4</sup>, P. L. Whitehouse<sup>4</sup>, A. A. Nyblade<sup>5</sup>, D. A.  
Wiens<sup>6</sup>, S. Anandakrishnan<sup>5</sup>, R. C. Aster<sup>7</sup>, A. D. Huerta<sup>8</sup>, A. J.  
Lloyd<sup>6</sup>, T. Wilson<sup>9</sup> and J. P. Winberry<sup>8</sup>

(1) School of Earth and Environment, The University of Leeds, Leeds, LS2 9JT, UK

(2) British Antarctic Survey, Natural Environment Research Council, Cambridge CB3  
0ET, UK

(3) Department of Earth and Planetary Science, Macquarie University, North Ryde,  
NSW 2109, Australia

(4) Department of Geography, Durham University, South Road, Durham, DH1 3LE,  
UK

(5) Department of Geosciences, The Pennsylvania State University, University Park,  
PA 16802, USA

(6) Department of Earth and Planetary Sciences, Washington University, St. Louis,  
MO 63160, USA

(7) Department of Geosciences, Colorado State University, Fort Collins, CO 80523,  
USA

(8) Department of Geological Sciences, Central Washington University, Ellensburg,  
WA 98926, USA

(9) School of Earth Sciences, Ohio State University, Columbus, OH 43210, USA

**Contents of this file**

- Figures S1 to S9
- Table S1

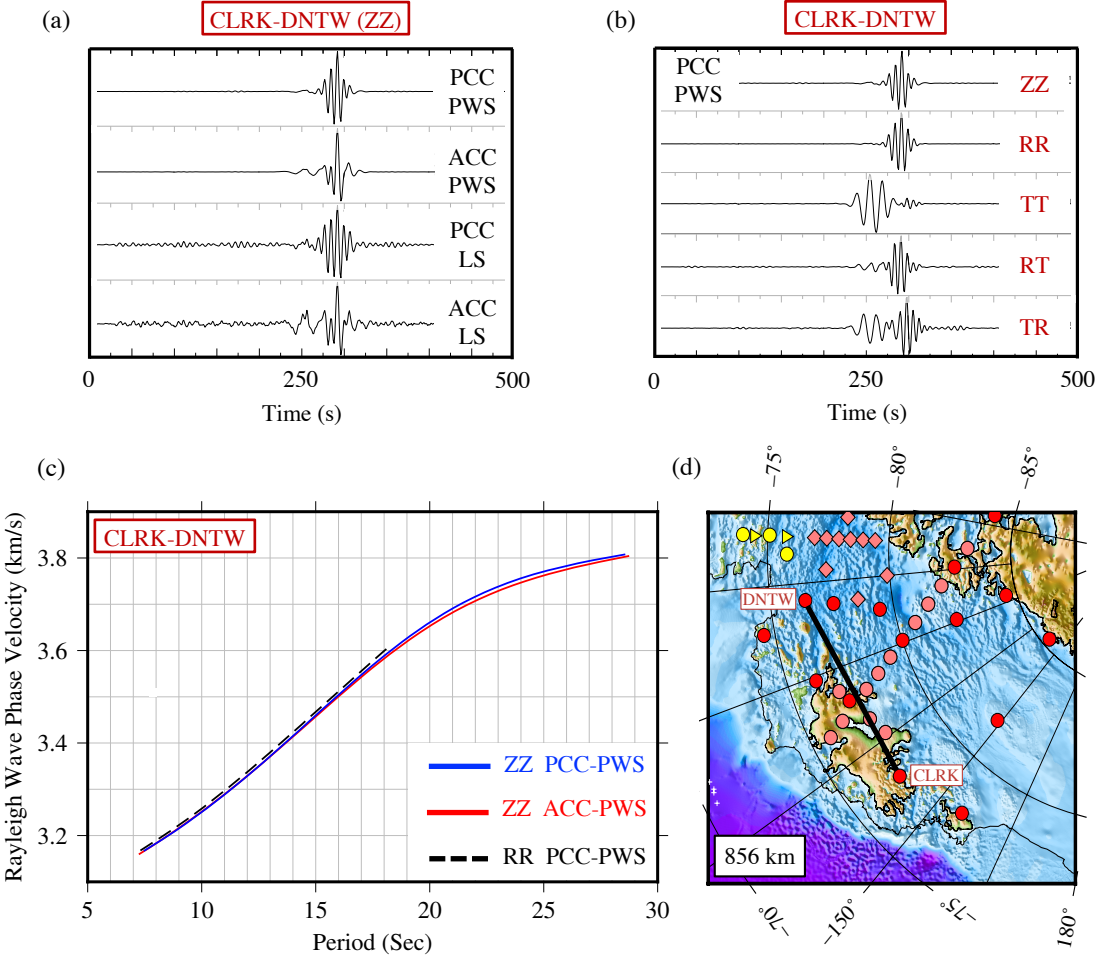


Figure S1: (a) Comparison of amplitude- and phase-based vertical-component symmetric cross-correlograms for POLENET station pair CLRK-DNTW with linear and time-frequency domain phase-weighted stacking. ACC, amplitude-based cross-correlation; PCC, phase-based cross-correlation; PWS, time-frequency domain phase weighted stacking; LS, linear stacking. In this study, we base our dispersion analysis on cross-correlograms calculated by phase-based coherence and time-frequency domain phase weighted stacking (PCC-PWS). (b) Vertical-vertical (ZZ), radial-radial (RR), transverse-transverse (TT), radial-transverse (RT) and transverse-radial (TR) symmetric cross-correlograms for CLRK-DNTW obtained by PCC-PWS. The ZZ and RR cross-correlograms both contain the Rayleigh wave, although the ZZ cross-correlogram generally has a higher signal-to-noise ratio. The TT cross-correlogram contains the faster Love wave. (c) Comparison of Rayleigh wave phase velocity dispersion inferred by automated frequency-time analysis (AFTAN) for ZZ and RR cross-correlograms calculated by PCC-PWS, and the ZZ cross-correlogram calculated by amplitude-based coherence and time-frequency domain phase weighed stacking (ACC-PWS). The velocities are consistent to within  $\sim 0.01$  km/s. The ZZ PCC-PWS cross-correlogram has a slightly higher signal-to-noise ratio than the RR PCC-PWS cross-correlogram, resulting in the differing period ranges of the respective dispersion curves. (d) Map of station locations.

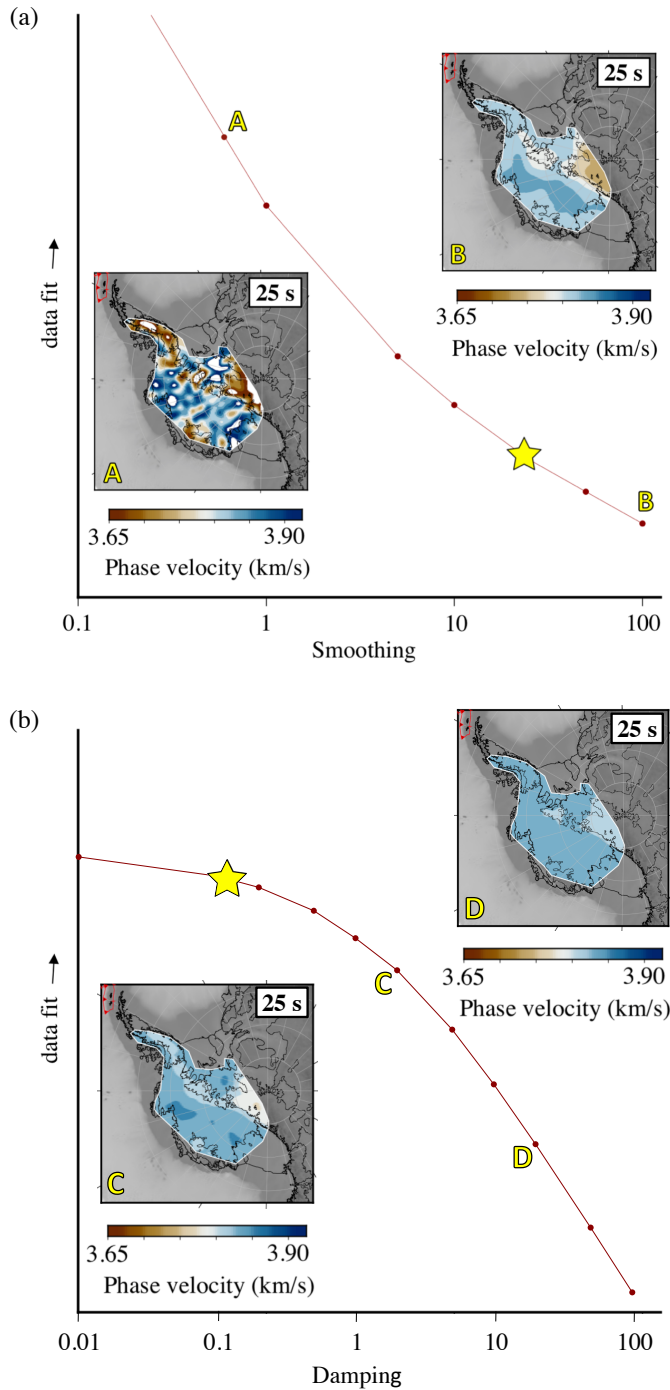


Figure S2: Trade-off curves illustrating choice of (a) smoothing and (b) damping regularisation for the tomography (stars). Each point represents a Rayleigh wave phase velocity model at a period of 25 s determined using particular smoothing/damping values. In (a) damping is held fixed at 0.1 while smoothing is varied and in (b) smoothing is held fixed at 25 while damping is varied. Under-smoothing (A) allows unrealistic fine scale structure to explain the data; over-smoothing (B) eliminates fine scale structure at the expense of data fitting. Over-damping (C and D) inhibits sufficient deviation from the (laterally homogeneous) starting model to explain the data. Models from the “knee” of the trade-off curves (stars) represent the best compromise between structural resolution and data fitting. All velocity models subsequently displayed were determined using a smoothing value of 25 and a damping value of 0.1.

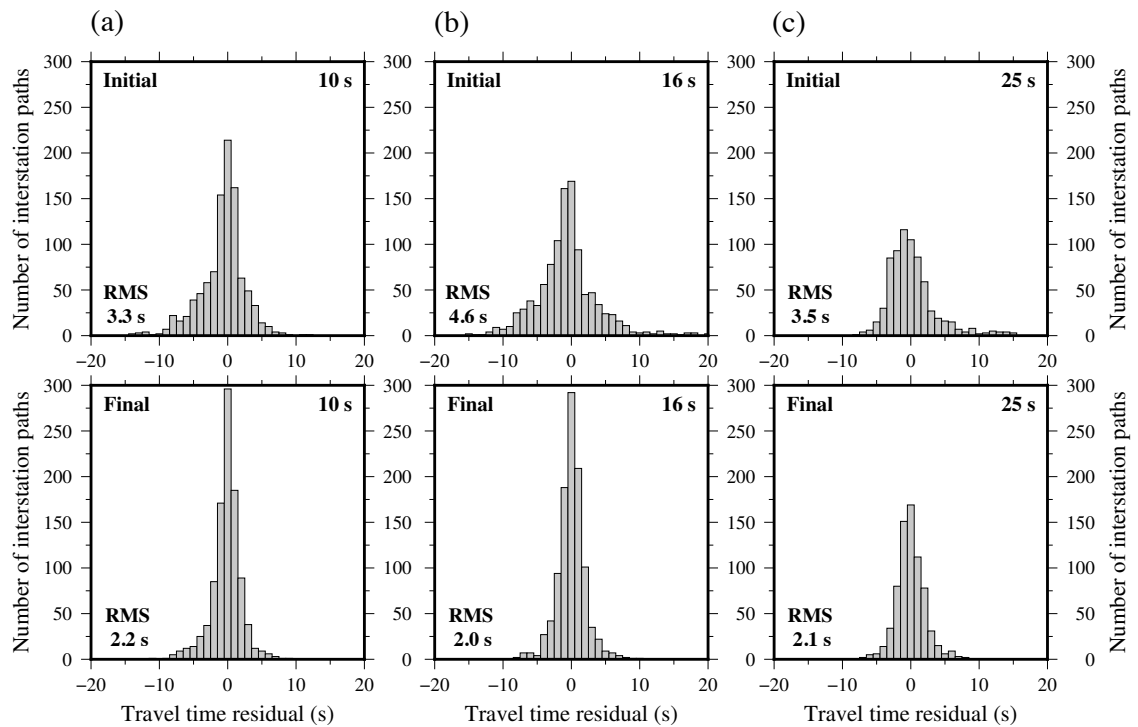


Figure S3: Histograms of travel time residuals for starting and final Rayleigh wave phase velocity models for periods (a) 10 s, (b) 16 s, and (c) 25 s. The root mean square (RMS) residual is shown in each case.

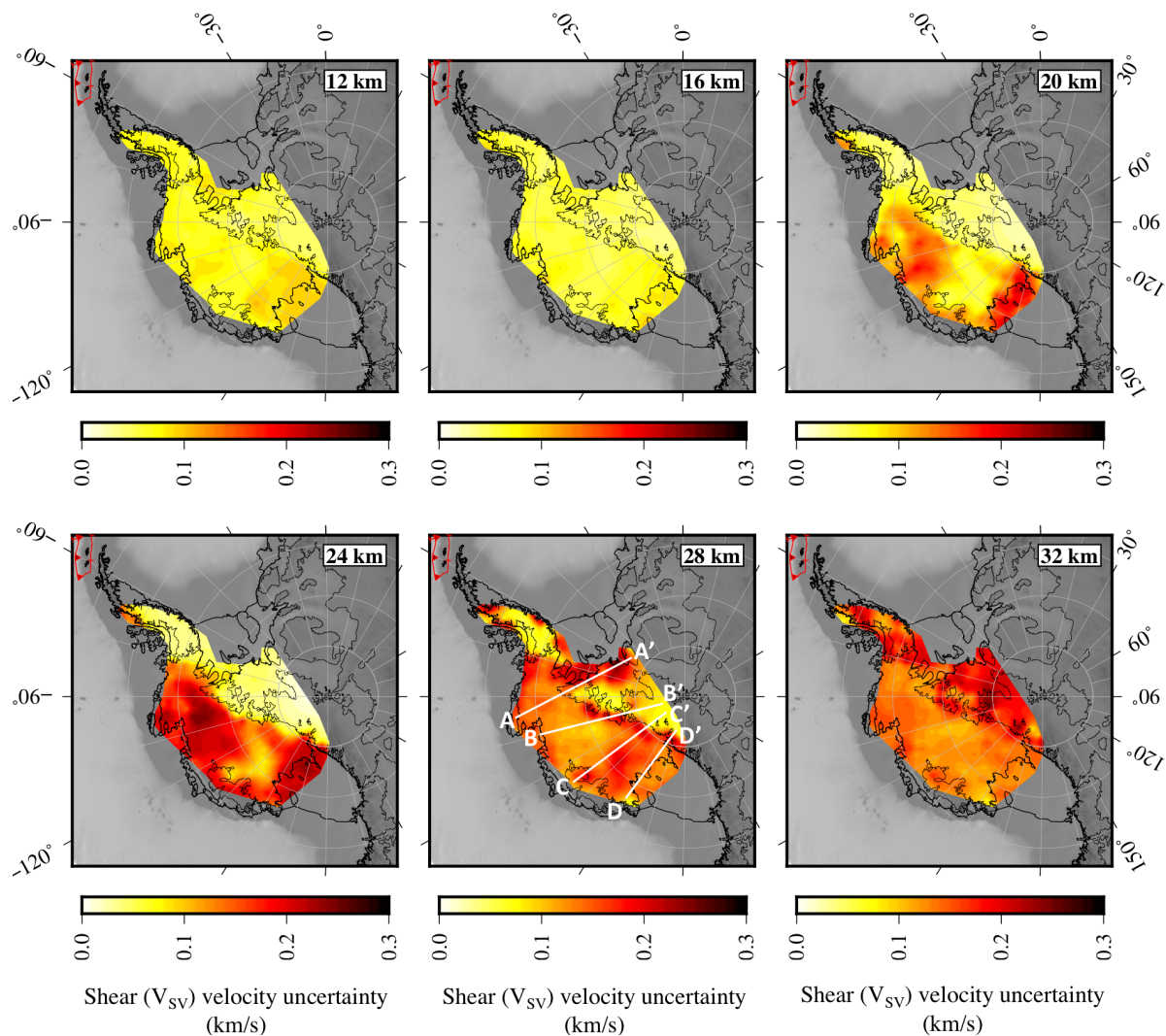


Figure S4: Shear wave velocity ( $V_{SV}$ ) standard deviation maps at a selection of depths. The locations of the vertical cross-sections shown in Figure S5 are superimposed on the 28 km depth map.

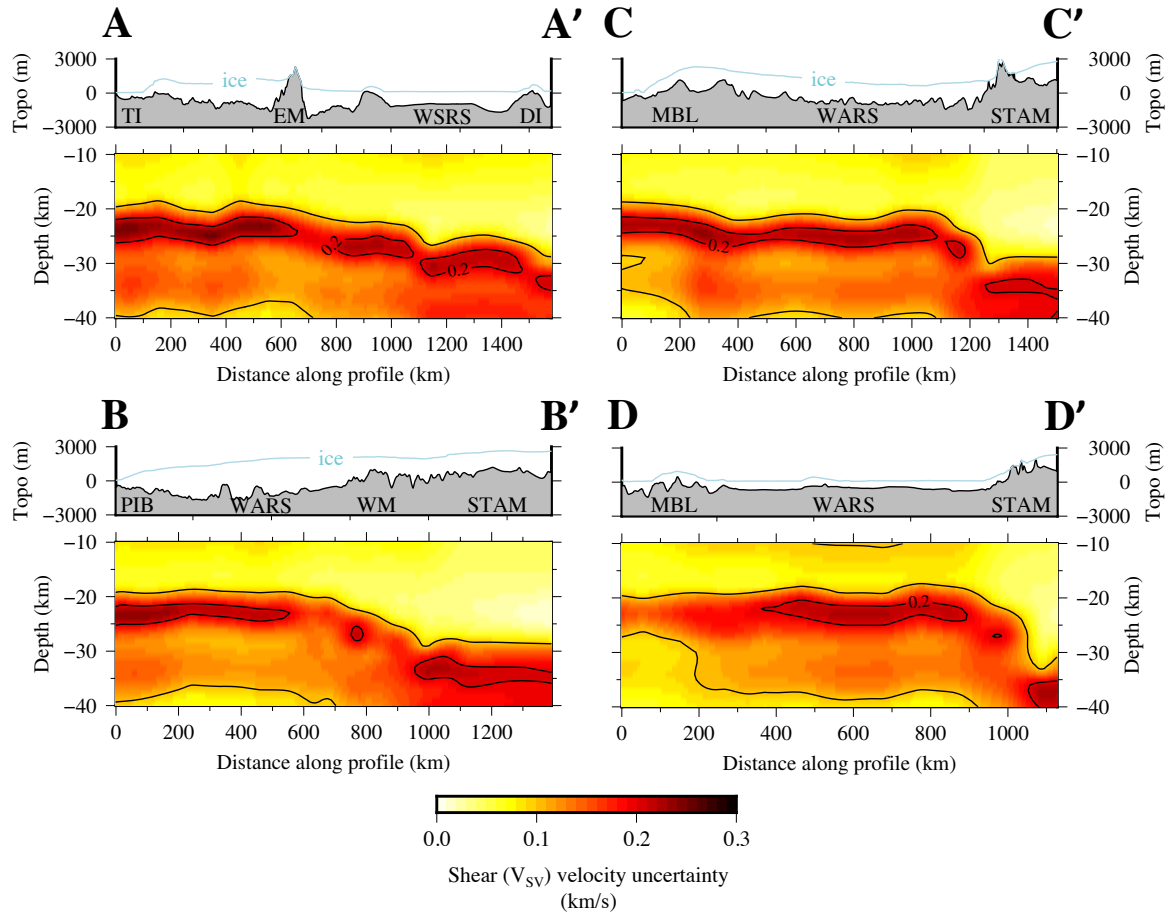


Figure S5: Vertical cross-sections showing the modelled mid-to-lower crustal and uppermost mantle shear wave velocity ( $V_{SV}$ ) standard deviation along the four profiles spanning the West Antarctic Rift System (WARS) located in Figure S4. The  $V_{SV}$  velocity uncertainties are contoured at 0.1 km/s intervals, with the 0.2 km/s contour labelled. Corresponding BEDMAP2 ice and bedrock topography (Topo) profiles are shown in each case. EM, Ellsworth Mountains; DI, Dufek Intrusion; MBL, Marie Byrd Land; PIB, Pine Island Bay; STAM, southern Transantarctic Mountains; TI, Thurston Island; WM, Whitmore Mountains; WSRS, Weddell Sea Rift System.

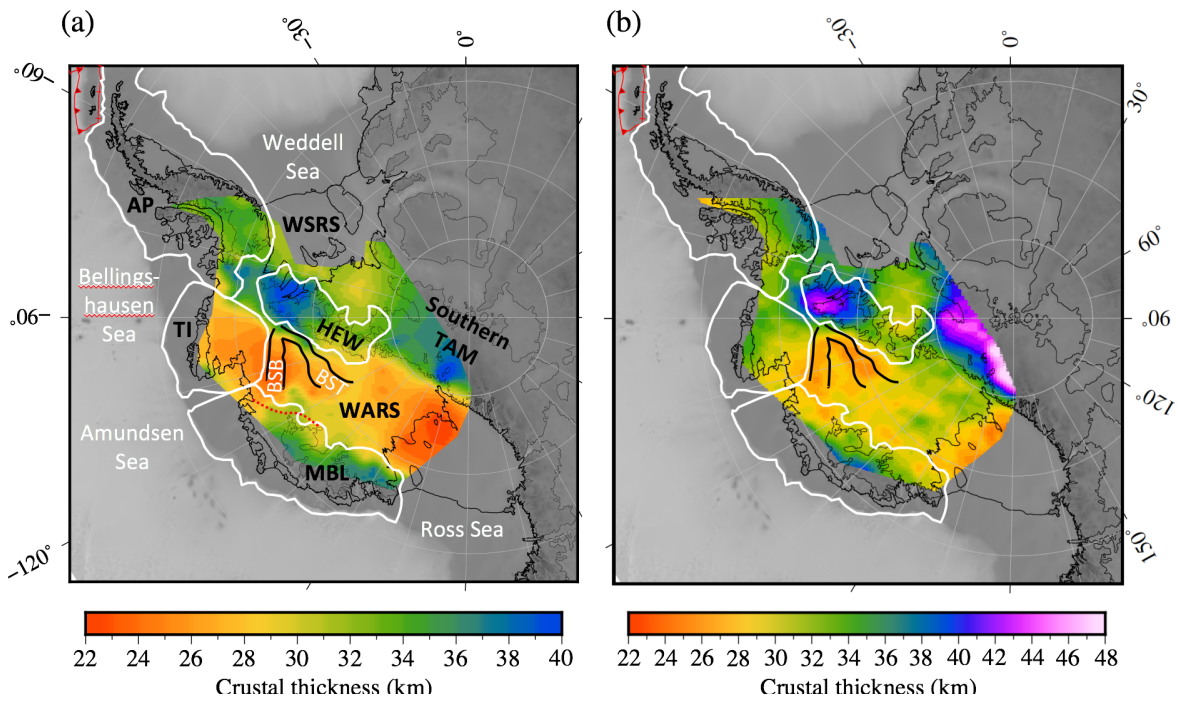


Figure S6: Comparison of crustal thickness models from (a) this study and (b) Shen et al. (2018) within overlap. In both cases antecedent Moho depths are translated to crustal thicknesses using BEDMAP2 bedrock topography data. Following Dalziel & Elliot (1982), white lines delineate major crustal blocks of West Antarctica (AP, Antarctic Peninsula; TI, Thurston Island; MBL, Marie Byrd Land; HEW, Haag Nunataks-Ellsworth Whitmore Mountains block). Other abbreviated features: BSB, Byrd Subglacial Basin; BST, Bentley Subglacial Trench; TAM, Transantarctic Mountains; WARS, West Antarctic Rift System; WSRS, Weddell Sea Rift System.

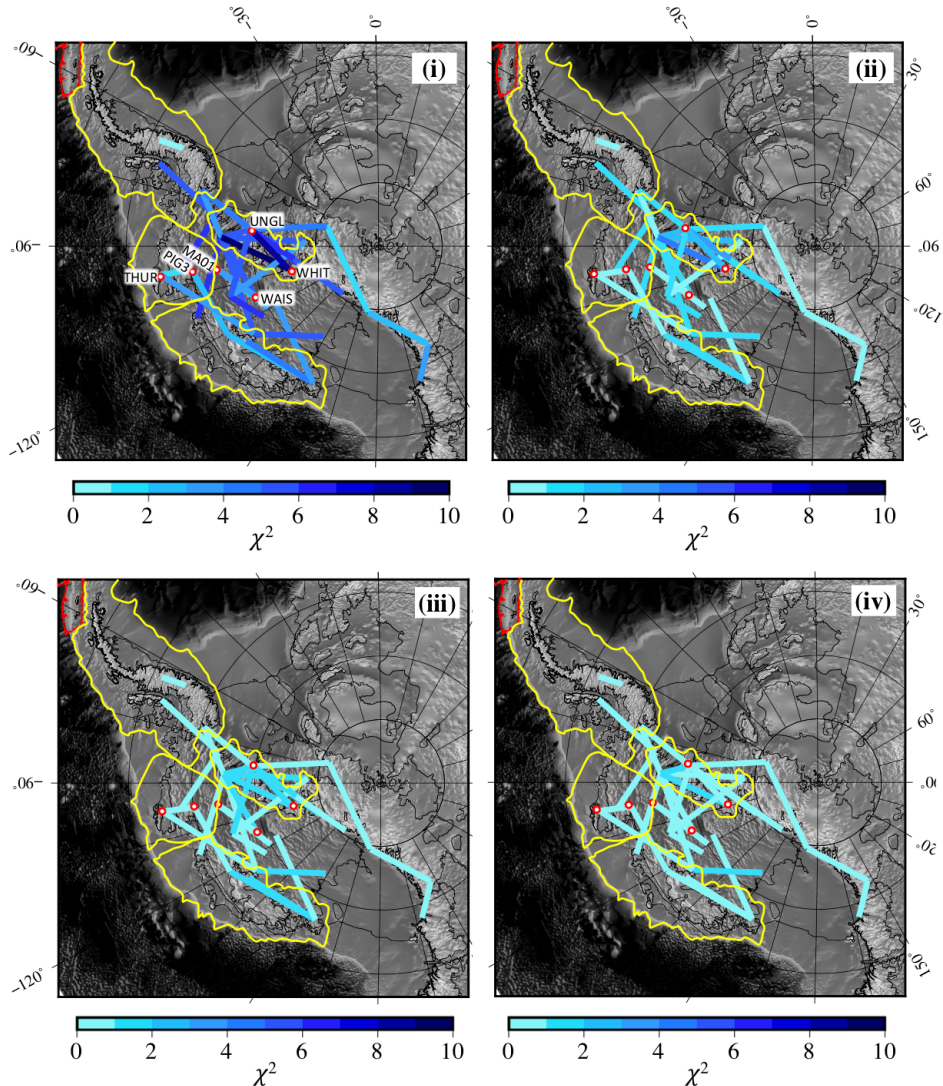


Figure S7: Observed versus predicted phase velocity dispersion  $\chi^2$  misfits for ensemble of interstations paths for scenarios: (i) isotropic uppermost mantle, isotropic crust (ii) anisotropic uppermost mantle, isotropic crust; (iii) anisotropic uppermost mantle, anisotropic lower crust; and (iv) anisotropic uppermost mantle, anisotropic mid and lower crust.

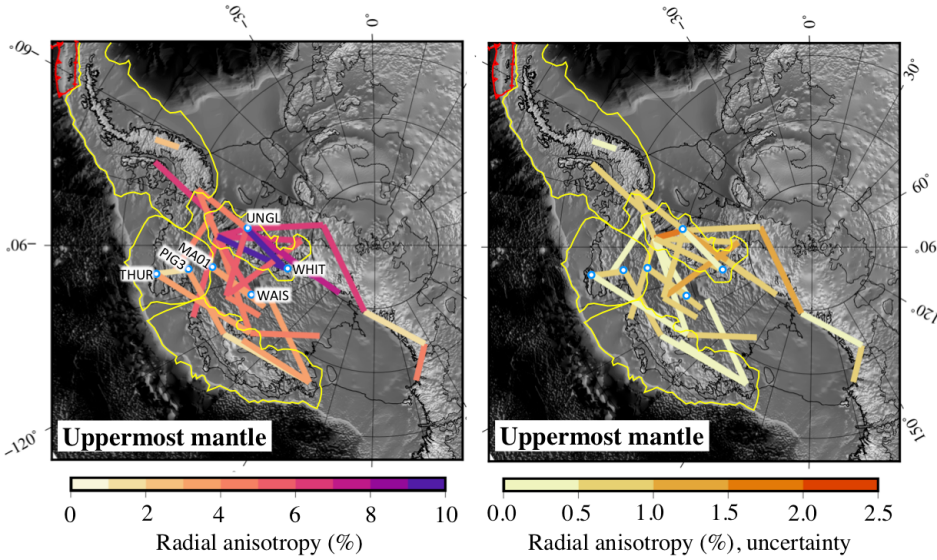


Figure S8: Interstation average % radial anisotropy resolving the Rayleigh-Love discrepancy (if any) for scenario (ii) anisotropic uppermost mantle, isotropic crust. The  $\chi^2$  misfits for this scenario are considerably worse than those scenarios permitting radial anisotropic crustal layers. The uncertainties are standard deviations derived from the final, best generations of anisotropic models from the genetic algorithm searches.

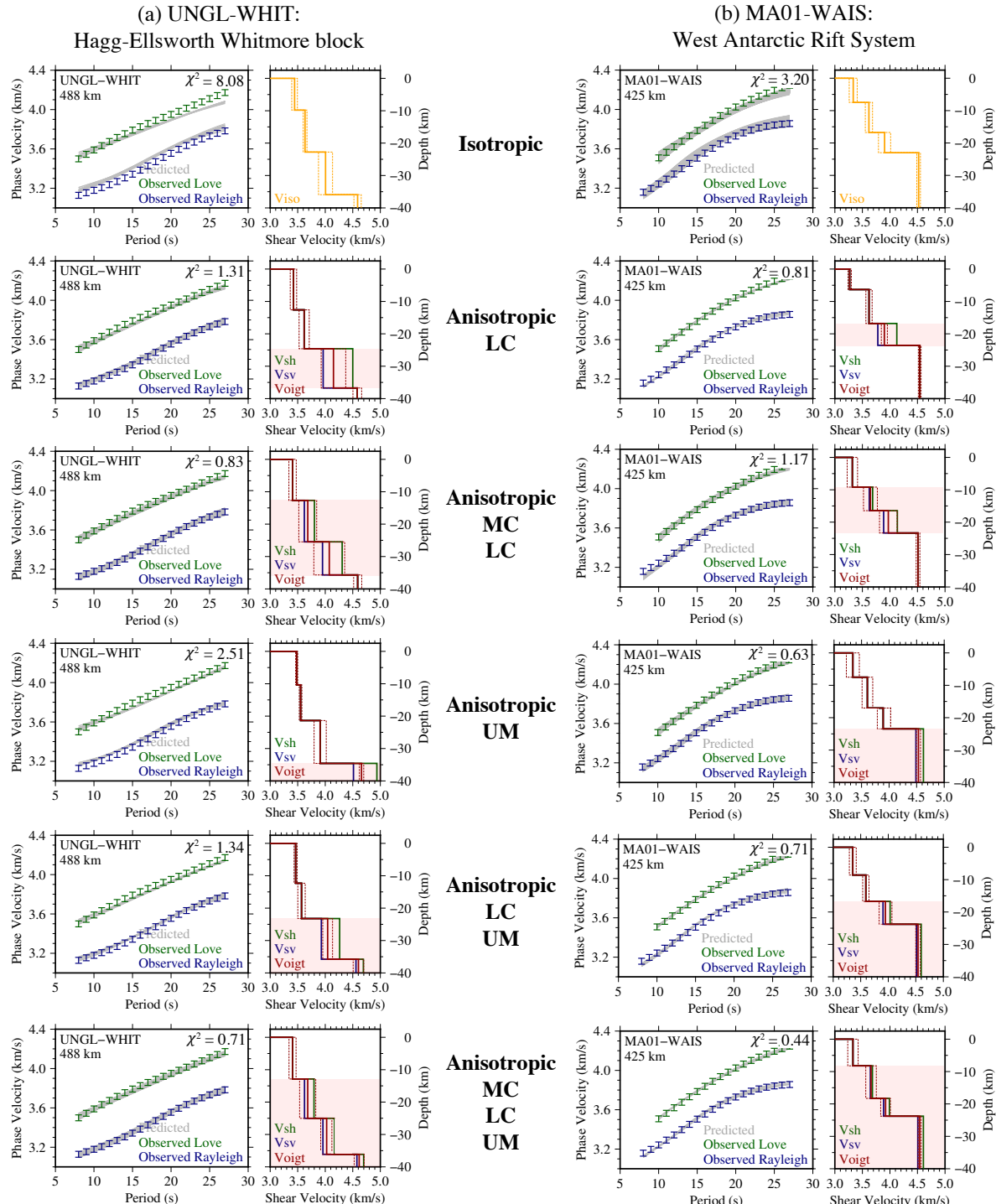


Figure S9:  $V_{SV}$ ,  $V_{SH}$ , Voigt average and isotropic interstation average velocity profiles for paths in central West Antarctica in the (a) Haag-Ellsworth Whitmore block and (b) West Antarctic Rift System inferred from corresponding interstation Rayleigh and Love wave phase velocity dispersion curves. Predicted dispersion curves are shown in grey and corresponding  $\chi^2$  misfits denoted. Confining radial anisotropy to the crust necessitates much stronger radial anisotropy (up to  $\sim 15\%$ ) to explain the Rayleigh-Love discrepancies to comparable  $\chi^2$  misfits as when the uppermost mantle is also modelled as radially anisotropic (as a visual aid, permitted radially anisotropic layers are shaded). MC, mid crust; LC, lower crust; UM uppermost mantle.

Table S1: UKANET seismic station coordinates and deployment durations.

| Station | Latitude (°) | Longitude (°) | Elevation (m) | Start      | End        |
|---------|--------------|---------------|---------------|------------|------------|
| ATOL    | -71.389670   | -68.870120    | 736.1         | 2017/01/10 | 2018/01/29 |
| BREN    | -72.674980   | -63.020940    | 1679.2        | 2017/01/19 | 2018/01/17 |
| ELSW    | -75.519370   | -85.707580    | 1199.9        | 2017/01/06 | 2018/01/21 |
| FOSS    | -71.314562   | -68.305435    | 84.8          | 2016/01/13 | 2016/02/09 |
| FOWL    | -76.892838   | -79.301124    | 1345          | 2016/02/13 | 2018/01/14 |
| KEAL    | -76.520375   | -85.699646    | 1038.5        | 2016/02/07 | 2017/01/06 |
| KIBB    | -75.276109   | -65.604903    | 1175          | 2016/01/16 | 2018/02/08 |
| PIG1    | -73.978274   | -97.574986    | 1046          | 2016/01/28 | 2018/01/23 |
| PIG2    | -74.455723   | -97.682966    | 986.4         | 2016/01/29 | 2016/12/25 |
| PIG3    | -75.084062   | -97.474449    | 655.5         | 2016/01/30 | 2018/01/23 |
| PIG4    | -75.759944   | -97.583041    | 762           | 2016/01/30 | 2016/12/21 |
| PIGD    | -75.802611   | -100.275845   | 841           | 2016/01/31 | 2018/01/25 |
| ROTH    | -67.520009   | -68.148847    | 265.2         | 2016/01/12 | 2017/01/14 |
| WELC    | -70.731810   | -63.827370    | 1548.4        | 2017/01/18 | 2018/01/06 |